

The Kalmag Model as a Candidate for IGRF-13

Julien Baerenzung (✉ baerenzung@gmx.de)

Universität Potsdam

Matthias Holschneider

Universität Potsdam

Johannes Wicht

Max-Planck-Institut für Sonnensystemforschung

Vincent Lesur

Institut de Physique du Globe

Sabrina Sanchez

Max-Planck-Institut für Sonnensystemforschung

Full paper

Keywords: Geomagnetic field, secular variation, assimilation, Kalman filter, machine learning

Posted Date: July 2nd, 2020

DOI: <https://doi.org/10.21203/rs.3.rs-38242/v1>

License:  This work is licensed under a Creative Commons Attribution 4.0 International License.

[Read Full License](#)

Version of Record: A version of this preprint was published on October 29th, 2020. See the published version at <https://doi.org/10.1186/s40623-020-01295-y>.

¹ The Kalmag model as a candidate for IGRF-13

Baerenzung Julien, Institute for Mathematics, University of Potsdam, Potsdam, Germany,
baerenzung@gmx.de

Holschneider Matthias, Institute for Mathematics, University of Potsdam, Potsdam, Ger-
many, matthias.holschneider@gmail.com

Wicht Johannes, Max Planck Institute for solar system research, Göttingen, Germany,
wicht@mps.mpg.de

Lesur Vincent, Institut de Physique du Globe, Paris, France, lesur@ipgp.fr

Sanchez Sabrina, Max Planck Institute for solar system research, Göttingen, Germany,
² sanchezs@mps.mpg.de

4 **Abstract**

5 We present a new model of the Geomagnetic field spanning the last 20 years and called Kalmag.
6 Deriving from the assimilation of CHAMP and SWARM vector field measurements, it separates the
7 different contributions to the observable field through parameterized prior covariance matrices. To make
8 the inverse problem numerically feasible it has been sequentialized in time through the combination of a
9 Kalman filter and a smoothing algorithm. The model provides reliable estimates of past, present and
10 future mean fields and associated uncertainties. The version presented here is an update of our IGRF
11 candidates, the amount of assimilated data has been doubled and the considered time window has been
12 extended from [2000.5, 2019.74] to [2000.5, 2020.33].

13 **Keywords**

14 Geomagnetic field, secular variation, assimilation, Kalman filter, machine learning

15 **Introduction**

16 The Earth's magnetic field has different sources. Classically, we distinguish internal and external sources
17 below and above the site where the field is measured. The three principal internal contributions are the
18 core field, the lithospheric field and the magnetic fields induced in the ocean or within the crust and upper
19 mantle. At large scales, the core field clearly dominates. Sustained by dynamo action in the liquid outer
20 core, it is predominantly dipolar, and varies on timescales ranging from months to millennia. Magnetic
21 field reversals, rare events on even longer times scales, are not considered here. On scales that correspond
22 to spherical harmonics (SH) degree beyond about 16, the core field is dominated by the lithospheric
23 field coming from the magnetized rocks of the crust. Since the Earth's mantle evolves extremely slowly,
24 the lithospheric field, can be considered as almost static. The external fields that are generated by
25 electrical currents in the ionosphere and in the magnetosphere, on the other hand can vary extremely
26 rapidly in time. Because the sources of the magnetospheric field (the ring current, the magnetopause
27 and magnetotail currents) are distant from the Earth, only its large scale contributions can be detected
28 by the low-orbiting magnetic satellites or by measurements on Earth's surface. This is not the case for
29 the ionospheric field which is generated closer to the Earth's surface. Because the dynamical behavior

30 of both ionospheric and magnetospheric fields is controlled by solar radiations (and also thermospheric
31 winds for the former), they are closely tied to solar activity, and can vary on very short timescales. The
32 external fields can therefore also induce a non negligible secondary field inside the electrically conducting
33 parts of the mantle, crust and oceans. Other potentially important induced fields are created because
34 the oceans move relative to the core fields.

35 Disentangling the different field contributions is a difficult task since they often overlap in spatial scale
36 and time scale. Many field models therefore resort to a regularization in space and time and only use
37 selected data. Some example are the CHAOS model series by *Olsen et al. (2006)*; *Finlay et al. (2016)*,
38 the comprehensive models by *Sabaka et al. (2002, 2015, 2018, 2020)*, the GRIMM models by *Lesur et al.*
39 *(2008, 2010, 2015)*, the POMME models by *Maus et al. (2005, 2010)*, or the gufm1 by *(Jackson et al.*
40 *(2000))*. The COV-OBS model by *(Gillet et al. (2013))* and the model recently proposed by *Ropp et al.*
41 *(2020)* are the only models that use a Bayesian approach instead of regularization. Usually only vector
42 field measurements taken during night time, under geomagnetic quiet conditions, and at low to mid
43 magnetic latitude are considered in order to minimize the contribution of fields created by currents in the
44 ionosphere or in auroral regions (field-aligned currents, DP2, auroral electrojet). Four main contributions
45 then remain, the core, the lithospheric, the magnetospheric and the induced fields. The core and the
46 lithospheric fields are usually treated as one internal source described by one set of spherical harmonics
47 coefficients. Small scale contributions beyond degree 16 or so are supposed to be of lithospheric origin
48 and are static in time while the larger scales represent the varying core field. Most of the models also
49 treat the induced fields and the magnetospheric field in a simplified way. The field induced by ocean
50 circulation and the the fields created in the magnetotail and the magnetopause are either neglected or
51 estimated separately. Only the magnetic field generated by the ring current and the respective induced
52 part then remain to be modeled. Yet, when assuming a 1d electrical conductivity profile for Earth's
53 mantle, the axisymmetric magnetospheric field and the related induced field can be parameterized by the
54 Disturbance short-time (Dst) index proposed by *Sugiura (1963)*. The Dst or other similar indices are
55 independently estimated from observations and can serve as model input.

56 To achieve an optimal separation of the different contributions, proper temporal parametrization of
57 the different sources is mandatory. In many models (CHAOS, GRIMM, CM, COV-OBS), the time
58 dependency of the core field is modeled by B-splines for an a priori fixed time step. This imposes a
59 relatively smooth evolution of the field, excluding the rapid variations attributed to external fields. In

60 addition, with algorithms based on regularized least square approaches, only the time derivatives of the
61 core field are penalized and no constraints on the morphology of the field itself are imposed. With the
62 COV-OBS model, *Gillet et al. (2013)* went a step further in characterizing a priori the spatio-temporal
63 behavior of the core field. They assumed that its dynamical evolution was controlled by a specific second
64 order auto regressive process which can reproduce the temporal statistical properties of the core field
65 which have been characterized with both observatory measurements (see *De Santis et al. (2003)*; *Lesur*
66 *et al. (2017)*) and numerical simulations of the geodynamo (see *Bouligand et al. (2016)*).

67 Although a good calibration of the temporal constraints is crucial for deriving magnetic field models
68 from observatory and satellite data, some key information can also be extracted from the morphology
69 and the spatial correlation structure of the different fields. *Holschneider et al. (2016)* have shown that
70 the use of appropriate parameterized correlation kernels, could greatly improve the separation of the
71 different components of the Earth's magnetic field. Working with observatory data for a single epoch,
72 they could detect the spatial signature of the core, lithospheric, magnetospheric and ionospheric fields.
73 Their Bayesian approach even allowed the quantification of uncertainties.

74 The Kalmag model we propose here combines such a technique with the sophisticated temporal correlation
75 functions introduced by *Gillet et al. (2013)*. Since ground based observatories and satellite missions
76 such as Oersted, SAC-C, Champ, or Swarm, have produced or are still generating a huge amount of
77 data, a block inversion would be numerically impossible. This is why we decided to assimilate the data
78 sequentially using a Kalman filter approach combined with a smoothing algorithm.

79 The article is organised as follows: in the next section, the data selection criteria and the modeling strategy
80 are detailed. We first present the different magnetic sources that are taken into account, we then show how
81 they are a priori characterized, and how such prior information can be modeled through auto regressive
82 processes. Based on these processes, the equations for the Kalman filter approach and the smoothing
83 algorithm are then given. Finally the methodology used to derive the different candidate models for
84 IGRF-13 is explained. In section **Results and discussion**, we present and discuss the outcomes of the
85 model. However, since the spatio-temporal prior characterization of each modeled magnetic source is
86 parameterized, we first show how these parameters are evaluated to be then incorporated in the model.
87 The article ends with some concluding remarks and perspectives to improve the Kalmag model.

88 **Methods**

89 **Data**

90 For the moment, the Kalmag model only uses the vector field measurements of the CHAMP and SWARM
91 low orbiting satellites. We sample CHAMP data at a rate of 1 datum every 5 seconds and only use
92 measurements where the vector field magnetometer (VFM) and the star tracker (STR) instruments were
93 functioning nominally. Very early in the SWARM mission (September 2014), the scalar magnetometers
94 on satellite Charlie stopped operating properly. We therefore only consider data from the Alpha and
95 Bravo satellites, using simultaneous sampling every 10 seconds. For the construction of the IGRF-13
96 candidate models, which we will refer to as the Kalmag candidates, a two times lower sampling rate was
97 used. Furthermore, we only used data up to 2019.74 for the Kalmag candidates but now extended this to
98 2020.33.

99 For latitudes between 60° north and south, only night time data are considered. Furthermore, indepen-
100 dently of the satellites locations, the following selection criteria are also applied:

- 101 • The z -component of the Interplanetary magnetic field(IMF) is positive .
- 102 • The geomagnetic activity index $Kp \leq 2^0$.

103 All in all the dataset is composed of 2 985 442 vector field measurements for CHAMP and 4 606 159 for
104 SWARM.

105 **Magnetic sources**

106 The different contributions to the observations are described in terms of magnetic sources of either
107 internal or external origin. Except for the field produced by field-aligned currents (b_{fac}), each of these
108 contributions b_i is deriving from a potential V_i :

$$b_i(r, \theta_s, \phi_s, t) = -\nabla V_i(r, \theta_s, \phi_s, t) . \quad (1)$$

109 For b_{fac} , we followed the study of *Waters et al.* (2001) and express it through the potential V_{fac} as
110 following:

$$b_{fac}(r, \theta_s, \phi_s, t) = -\mathbf{r} \times \nabla V_{fac}(r, \theta_s, \phi_s, t) . \quad (2)$$

111 Note that depending on the source, the spherical coordinate system $\{r, \theta_s, \phi_s\}$ the magnetic field is
112 expressed in may differ. Here four types of systems are used: geographic (GEO), magnetic (MAG), solar
113 magnetic (SM), and geocentric solar magnetospheric (GSM).

114 Each potential V_i is then expanded in spherical harmonics (SH), which for internal and external sources

115 respectively read:

$$V_i^I(r, \theta_s, \phi_s, t) = a_i \sum_{\ell \leq \ell_{max}} \sum_{m=-\tilde{m}}^{m=\tilde{m}} \left(\frac{a_i}{r}\right)^{\ell+1} g_{i,\ell,m}^I(t) Y_{\ell,m}(\theta_s, \phi_s), \quad (3)$$

$$V_i^E(r, \theta_s, \phi_s, t) = a_i \sum_{\ell \leq \ell_{max}} \sum_{m=-\tilde{m}}^{m=\tilde{m}} \left(\frac{r}{a_i}\right)^\ell g_{i,\ell,m}^E(t) Y_{\ell,m}(\theta_s, \phi_s). \quad (4)$$

116 The $Y_{\ell,m}$ are Schmidt semi-normalized spherical harmonics of degree ℓ and order m , ℓ_{max} is the maximum
 117 of degree expansion, a_i is a reference radius, and $g_{i,\ell,m}(t)$ (later referred as g_i) are the spherical harmonics
 118 coefficients expressed at a_i . \tilde{m} is the maximum order considered for the spherical harmonics expansion.
 119 A complete expansion, referred as standard, requires $\tilde{m} = \ell$. However some sources, in particular external
 120 fields, are known to have a strong zonal signature (see *Finlay et al. (2017)*), and are therefore restricted
 121 to either zonal spherical harmonics modes with $\tilde{m} = 0$ or to an expansion we refer as zonal iso where
 122 $\tilde{m} = 1$.

Table 1. Magnetic sources considered in the model. The second column corresponds to the coordinate system each field is expressed in. GEO stands for geographic, SM for solar magnetic, MAG for magnetic and GSM for geocentric solar magnetospheric. ℓ_{max} is the maximum degree of the SH expansion, for the three following types of decomposition: standard with $m = [-l, l]$, zonal with $m = 0$ and zonal iso where $m = \{0, 1, -1\}$.

Source	Coordinate	ℓ_{max}	SH decompos- tion
Core g_c	GEO	20	Standard
Lithospheric g_l	GEO	76	Standard
Remote magnetospheric g_{rm}	GSM	1	Zonal
Close magnetospheric g_m	SM	15	Zonal
Fluctuating magnetospheric g_{fm}	SM	15	Zonal iso
Residual ionospheric/ induced g_{ii}	MAG	50	Zonal iso
Field-aligned currents g_{fac}	SM	15	Zonal iso

123 The Kalmag model is composed of 7 sources. 3 of them are of internal origin, the core field (g_c), the
 124 lithospheric field (g_l) and the induced / residual ionospheric field (g_{ii}). g_c and g_l are expressed in the
 125 geographic coordinate system and expanded in SH with the standard decomposition. g_{ii} is expressed in

126 the solar magnetic coordinate system and its SH decomposition is restricted to $\tilde{m} = 1$ (zonal iso). 3
 127 sources are used to characterize the magnetospheric field. A remote one (g_{rm}) in GSM which is purely
 128 dipolar and zonal, and 2 close sources (g_m and g_{fm}) expressed in the SM coordinate system. g_m is purely
 129 zonal and it is accompanied by g_{fm} a fluctuating source expanded with the zonal iso SH decomposition.
 130 Finally, the source associated with field-aligned currents is expressed in the SM coordinate system and
 131 restricted to the zonal iso SH expansion. The nature of the 7 sources composing the Kalmag model, the
 132 coordinate system they are expressed in, and their spherical harmonics truncation level are listed in table
 133 1.

134 **Prior characterization of spatial and temporal correlations**

135 To obtain an optimal separation of the various contributions to geomagnetic observations, proper prior
 136 characterization of the different magnetic sources is mandatory. Following the studies of *Hulot and Le*
 137 *Mouél* (1994); *Gillet et al.* (2013); *Holschneider et al.* (2016), full space-time covariance matrices are used
 138 to characterize each magnetic source g_i . Assuming that $E[g_i] = 0$ the latter read:

$$E \left[\begin{pmatrix} g_i(t) \\ g_i(t + \Delta t) \end{pmatrix} (g_i(t)^T g_i(t + \Delta t)^T) \right] = \begin{pmatrix} \Sigma_{g_i}^\infty & c_i(\Delta t) \Sigma_{g_i}^\infty \\ \Sigma_{g_i}^\infty c_i(\Delta t)^T & \Sigma_{g_i}^\infty \end{pmatrix}, \quad (5)$$

139 where the matrix $\Sigma_{g_i}^\infty$ corresponds to the stationary spatial covariance, and $c(\Delta t)$ is a temporal correlation
 140 matrix depending on the time lag Δt . $\Sigma_{g_i}^\infty$ is assumed to derive from energy spectra $E_i^\infty(\ell, a_i)$, expressed
 141 at given radii a_i , such as:

$$\begin{aligned} \Sigma_{g_i}^\infty(\ell, m, \ell', m', r = a_i) &= E[g_i(\ell, m) g_i(\ell', m')] \\ &= \frac{E_i^\infty(\ell, a_i)}{N_m F(\ell)} \delta(\ell - \ell') \delta(m - m') \end{aligned} \quad (6)$$

142 where N_m is the number of modeled spherical harmonics coefficients per degree ℓ , and F is the pre-factor
 143 of the energy spectra given by $F(\ell) = \ell + 1$ and $F(\ell) = \ell$ for internal and external sources respectively.
 144 Two types of spectra are used for the model, flat ones, with $E_i^\infty(\ell) = A_i^2$ where A_i is a magnitude, and
 145 spectra of the form $E_i^\infty(\ell) = A_i^2(2\ell + 1)F(\ell)$, referred as C-based spectra, making equation 6 equivalent
 146 to the correlation kernels proposed by *Holschneider et al.* (2016). Only 2 sources are characterized by a
 147 flat spectrum, the core field and the induced / residual ionospheric field. This choice was driven by the
 148 evaluation we performed in section **Parameter estimation** where such a parametrization enabled us to
 149 better explain the data.

150 Note that the covariance matrices of equation 6 are diagonal. More complex covariance structures could

151 be used, accounting for the correlations between different magnetic modes as they appear in dynamo
 152 simulations for instance (see *Sanchez et al. (2019)*). However, the large amount of data available for this
 153 study are sufficient to properly constrain the model and permits such general prior assumptions.

154 Temporal constraints are prescribed by the type of correlation functions introduced by *Gillet et al. (2013,*
 155 *2015)* in the context of geomagnetic modeling. They are deriving from the auto-regressive processes
 156 further discussed below, and read:

$$c_i(\Delta t) = \exp[-|\Delta t|/\tau_i(\ell)] \quad (7)$$

157 for first order processes and:

$$c_i(\Delta t) = (1 + (|\Delta t|/\tau_i(\ell))) \exp[-(|\Delta t|/\tau_i(\ell))] \quad (8)$$

158 for second order processes. $\tau_i(\ell)$ are scale dependent characteristic timescales. For the core field,
 159 *Christensen and Tilgner (2004); Lhuillier et al. (2011)* have shown that its characteristic timescales
 160 $\tau_c(\ell)$ could be approximated by a power law such as $\tau_c(\ell) = \tau_{SV}\ell^{-1}$ with τ_{SV} the secular variation
 161 timescale. In this study we decided to use such a power law description of τ_i for each magnetic source
 162 except for the lithospheric field, leading to:

$$\tau_i(\ell) = M_i\ell^{-\alpha_i} \quad (9)$$

163 with amplitudes M_i and exponent α_i . In our parametrization of the problem we therefore use four main
 164 parameters to characterize each source: 1) the amplitude A_i , 2) the (virtual) source radius a_i , 3) the
 165 time scale amplitude M_i and 4) the time scale slope α_i . In addition, because of the specific behavior
 166 of the dipole components, for the core field (see *Christensen and Tilgner (2004); Lhuillier et al. (2011)*)
 167 but also for the magnetospheric sources (see *Sugiura (1963); Finlay et al. (2016)*), the spatial and
 168 temporal properties of each source's dipole (except for the lithospheric field) is treated separately from
 169 the remaining SH coefficients. These parameters are directly estimated with a subsample of the dataset
 170 following the procedure described in section **Parameter estimation**.

171 **Sequentialization**

172 For the following developments, the parameters characterizing the prior covariance structures (A_i , a_i ,
 173 M_i and α_i) are assumed to be known. Instead of performing a full Bayesian block inversion with the
 174 covariance matrices given by equation 5 as a prior information, we proceed in a recursive way through
 175 the Kalman filter approach proposed by *Kalman (1960)*. To do so, dynamical equations are required

176 to forecast the statistical properties of the different modeled sources. As previously mentioned, the
 177 covariance structures we wish to a priori impose are deriving from autoregressive processes. In their
 178 continuous form the latter are given for first and second orders by respectively:

$$\partial_t g_{i,\ell,m}(t) + \frac{1}{\tau_i(\ell)} g_{i,\ell,m}(t) = \sigma_{i_1}(\ell) \dot{\omega}_{i_1}(t) \quad (10)$$

$$\partial_t^2 g_{i,\ell,m}(t) + \frac{2}{\tau_i(\ell)} \partial_t g_{i,\ell,m}(t) + \frac{1}{\tau_i^2(\ell)} g_{i,\ell,m}(t) = \sigma_{i_2}(\ell) \dot{\omega}_{i_2}(t) \quad (11)$$

179 where $\dot{\omega}_{i_1}(t)$ and $\dot{\omega}_{i_2}(t)$ are Gaussian white noises scaled by the factors $\sigma_{i_1}(\ell)$ and $\sigma_{i_2}(\ell)$ respectively.

180 These equations have explicit solutions which satisfy:

$$z_i(t + \Delta t) = F_i(\Delta t) z_i(t) + \xi_i(t, \Delta t) \quad (12)$$

181 where the temporal Gaussian white noise ξ_i is spatially (in terms SH coefficients) characterized by the
 182 distribution $\mathcal{N}(0, \Sigma_{z_i}^\infty - F_i \Sigma_{z_i}^\infty F_i^T)$, and where Δt can either be positive or negative.

183 For magnetic sources characterized by first order auto regressive processes, $z_i = g_i$ and F_i is given by:

$$F_i(\ell, \Delta t) = \exp[-|\Delta t|/\tau_i(\ell)]. \quad (13)$$

184 The core field evolution is prescribed by a second order auto regressive process, so the field itself and the
 185 secular variation are dynamically tied together. In this case, $z_i = (g_i, \partial_t g_i)^T$ and:

$$F_i(\ell, \Delta t) = \begin{pmatrix} 1 + |\Delta t|/\tau_i(\ell) & \Delta t \\ -\Delta t/\tau_i^2(\ell) & 1 - |\Delta t|/\tau_i(\ell) \end{pmatrix} \exp[-|\Delta t|/\tau_i(\ell)]. \quad (14)$$

186 Note that the covariance matrix of the core field when the later is assumed to be in a stationary state is
 187 given by:

$$\Sigma_{g_c, \partial_t g_c}^\infty = \begin{pmatrix} \Sigma_{g_c}^\infty & 0 \\ 0 & \Sigma_{g_c}^\infty / \tau_c^2(\ell) \end{pmatrix}, \quad (15)$$

188 as shown by *Hulot and Le Mouél* (1994).

189 **Sequential assimilation**

190 The Kalmag model consists in a vector \mathbf{z} containing the spherical harmonics coefficients of every magnetic
 191 source (including the SH expansion of the secular variation). With the decomposition detailed in section

192 **Magnetic sources**, \mathbf{z} contains 6624 SH coefficient entries. Its evaluation is performed with a Kalman
 193 filter algorithm which proceeds sequentially in two steps. In the first step, the forecast, the evolution of
 194 the mean model $E[\mathbf{z}]$ together with its associated covariance matrix $\Sigma_{\mathbf{z}}$ are predicted until observations

195 become available. In the second step, namely the analysis, the model is corrected to better reflect the
 196 data through a Bayesian inversion.

197 To predict the simultaneous evolution of the different magnetic sources with the auto-regressive processes
 198 presented in the previous section, a matrix \mathbf{F} containing all the matrices F_i , and a matrix $\tilde{\Sigma} =$
 199 $\Sigma^\infty - \mathbf{F}\Sigma^\infty\mathbf{F}^T$ characterizing the white noise of the complete evolution model, are constructed. The
 200 evolution of the mean model and its covariance from time step $k - 1$ to step k is then given by the
 201 forecast:

$$E[\mathbf{z}_{k|k-1}] = \mathbf{F}_{k-1}E[\mathbf{z}_{k-1}] \quad (16)$$

$$\Sigma_{\mathbf{z}_{k|k-1}} = \mathbf{F}_{k-1}\Sigma_{\mathbf{z}_{k-1}}\mathbf{F}_{k-1}^T + \tilde{\Sigma}. \quad (17)$$

202 At iteration k , whenever measurements are available, the model is updated with the formulations:

$$\mathbf{K}_k = \Sigma_{\mathbf{z}_{k|k-1}}\mathbf{H}_k^T \left(\mathbf{H}_k\Sigma_{\mathbf{z}_{k|k-1}}\mathbf{H}_k^T \right)^{-1} \quad (18)$$

$$E[\mathbf{z}_{k|\mathbf{d}_k}] = E[\mathbf{z}_{k|k-1}] + \mathbf{K}_k (d_k - \mathbf{H}_k E[\mathbf{z}_{k|k-1}]) \quad (19)$$

$$\Sigma_{\mathbf{z}_{k|\mathbf{d}_k}} = (\mathbf{I} - \mathbf{K}_k\mathbf{H}_k)\Sigma_{\mathbf{z}_{k|k-1}} \quad (20)$$

203 where \mathbf{K}_k is the Kalman gain matrix and \mathbf{H}_k is the operator projecting the model to the data d_k at
 204 iteration k . Note that the time step of the algorithm has been set to $\Delta t = 30$ minutes. Within this time
 205 window most of the magnetic sources are assumed to be static. However, the spatio-temporal correlations
 206 of the FAC source as well as the non dipolar part of the close magnetospheric field are modeled within
 207 this time window for reasons detailed in section **Parameter estimation**.

208 Smoothing

209 With the Kalman filter algorithm, one gets access to the distribution $p(\mathbf{z}_k|\mathbf{d}_k)$, where \mathbf{d}_k corresponds
 210 to all the measurements up to iteration k . To obtain $p(\mathbf{z}_k|\mathbf{d})$ the posterior distribution of the model
 211 at iteration k given the entire dataset \mathbf{d} , one can apply a smoothing algorithm. In this study we chose
 212 the formulation of *Rauch et al.* (1965). Starting at the last iteration of the Kalman filter algorithm, the
 213 smoothing algorithm performs iteratively backward in time accordingly to the following steps:

$$\mathbf{G}_{k-1} = \Sigma_{\mathbf{z}_{k-1}|\mathbf{d}_{k-1}}\mathbf{F}_k^T\Sigma_{\mathbf{z}_{k|k-1}}^{-1} \quad (21)$$

$$E[\mathbf{z}_{k-1}|\mathbf{d}] = E[\mathbf{z}_{k-1}|\mathbf{d}_{k-1}] + \mathbf{G}_{k-1} (E[\mathbf{z}_k|\mathbf{d}] - E[\mathbf{z}_k|\mathbf{d}_{k-1}]) \quad (22)$$

$$\Sigma_{\mathbf{z}_{k-1}|\mathbf{d}} = \Sigma_{\mathbf{z}_{k-1}|\mathbf{d}_{k-1}} + \mathbf{G}_{k-1} (\Sigma_{\mathbf{z}_k|\mathbf{d}} - \Sigma_{\mathbf{z}_k|\mathbf{d}_{k-1}}) \mathbf{G}_{k-1}^T. \quad (23)$$

214 The combination Kalman filter-smoothing algorithm was also chosen by *Ropp et al.* (2020) for their
 215 IGRF-13 main field candidate. However, their approach differs from ours in many aspects. In particular,
 216 their core field evolution is prescribed by an Euler scheme and they estimate the secular variation through
 217 the fluctuation of the field within 3 month time windows. Here the secular variation is tied to the core
 218 field evolution through the AR2 process. Its evaluation is therefore achieved by through dynamical link
 219 and correlation with the core field.

220 Candidate models

221 The models that we proposed as candidates for the IGRF-13 in 2020.0 are the Kalman filter solutions
 222 after the last analysis step in 2019.74 (September the 27th). This solution was forwarded in time until
 223 2020.0 using the forecast of equations 16 and 17 with propagators \mathbf{F} and noise covariance $\tilde{\Sigma}$ for a time step
 224 of $\Delta t = 0.26yr$. The secular variation candidate is the mean secular variation estimation in 2020.0. The
 225 associated uncertainties were obtained by taking the square root of the diagonal elements of the covariance
 226 matrix $\Sigma_{\partial_t g_c}(t = 2020)$, providing the standard deviation corresponding to each SH coefficients of $\partial_t g_c$.

227 Our internal field candidate model in 2020.0 contains the sum of the mean core field and the mean
 228 lithospheric field at this epoch ($E[g_c] + E[g_l]$). The uncertainties estimates were derived from the
 229 covariance matrix $\Sigma_{g_c+g_l} = \Sigma_{g_c} + \Sigma_{g_l} + \Sigma_{g_{cl}} + \Sigma_{g_{cl}}^T$ in 2020.0, where $\Sigma_{g_{cl}}$ is the cross covariance between
 230 the core field and the lithospheric field. The square root of each diagonal elements of $\Sigma_{g_c+g_l}$ provides the
 231 standard deviation associated with $E[g_c] + E[g_l]$.

232 Finally, our candidate for the DGRF 2015.0 model was constructed as our 2020.0 internal field model,
 233 except that the core and the lithospheric fields were taken from the smoothing solution.

234 The Kalmag model presented below uses additional data from September 27 2019 until April 2020.

235 Results and discussion

236 Parameter estimation

237 In this section the parameters characterizing the different magnetic sources, the spectra amplitudes A_i
 238 and radius a_i , the characteristic timescales magnitudes M_i and slopes α_i are evaluated. The spectral
 239 resolution as well as the spherical harmonics expansion chosen to model the different fields are a priori
 240 imposed (see table 1). The spherical harmonics coefficients of the different sources at the different models
 241 time are calculated with our Kalman filter scheme with a subsample of the data between 2001.0 and 2018.0.
 242 In order to avoid measurements taken by CHAMP or SWARM during strongly magnetically disturbed

243 epochs, and such as no permanent bias due to the static part of the magnetic field generated by the ring
244 current remain in the data, measurements deviating by 60 nT in intensity from the CHAOS-6 internal
245 field model and a yearly estimation of a degree 1 external field expressed in the SM coordinate system
246 are removed from the set. After this operation, a sample of $N_{est} = 247453$ vector field measurements
247 regularly spaced in time is kept and used to estimate the parameters for the different sources.
248 This estimation procedure is initialized with a first guess for each parameter. For internal (or external)
249 sources, radii lower (or larger) than the Earth’s radius are chosen. For the external sources we assume a
250 characteristic time scale of one day and set the slopes associated with $\tau_i(\ell)$ to $\alpha_i = 0$. The same is used for
251 the induced and the ionospheric field. The lithospheric field, on the other hand, is assumed to be static.
252 As mentioned above, several authors report that the core field time scales are inversely proportional to
253 the spherical harmonics degree (except for the axial dipole), implying $\alpha_c = 1$. We start our estimation
254 with an initial guess of $\alpha_c = 0$ and $M_c = 30$ years and check whether we nevertheless recover the results
255 suggested by the other authors.

256 Given a set of parameters, we perform the Kalman filter assimilation described above with the data
257 subset. Before each analysis step we can calculate how well the model predict the data with the relation:

$$F_k^{pred} = -\log \left| \mathbf{H}_k \boldsymbol{\Sigma}_{\mathbf{z}_{k|k-1}} \mathbf{H}_k^T \right| - (d_k - \mathbf{H}_k E[\mathbf{z}_{k|k-1}])^T \left(\mathbf{H}_k \boldsymbol{\Sigma}_{\mathbf{z}_{k|k-1}} \mathbf{H}_k^T \right)^{-1} (d_k - \mathbf{H}_k E[\mathbf{z}_{k|k-1}]) . \quad (24)$$

258 Summing F_k^{pred} over all k iterations provides the measure for the model compatibility with the data.
259 We randomly explore the multi-dimensional parameter space, seeking to maximise $\sum_k F_k^{pred}$. The final
260 values from this parameter search are given in table 2. Remember that for each source with the exception
261 of the lithospheric field, we distinguish between the dipole spatial and time scales and the spatial and
262 time scales of the other harmonics.

263 Figure 1 shows the static energy spectra projected at the Earth’s surface that define the spatial covariance
264 structure of equation 6 for the optimal parameters. A comparison with the CHAOS-6.9 core field model
265 of *Finlay et al.* (2016) (black circles) and the LCS-1 lithospheric field model of *Olsen et al.* (2017)
266 demonstrates the close agreement. The other internal source taken into account in our model is the
267 residual ionospheric/ induced field (g_{ii}). It is dipole dominated and exhibits an almost flat spectrum at
268 the Earth’s surface as illustrated by the blue line in figure 1. Without the restriction to magnetically quiet
269 data, this source would be much more energetic. This is also the case for the magnetic field generated
270 by field-aligned currents (g_{fac}), which reaches a similar amplitude as g_{ii} (dashed line in figure 1). The

Table 2. Magnetic sources parameters as described in section **magnetic sources**. The prior spatial covariance matrices are deriving from energy spectra expressed at some radii a_i which are either flat with $E_i^\infty(\ell) = A_i^2$ or of the C-based type with the form $E_i^\infty(\ell) = A_i^2(2\ell+1)F(\ell)$ where $F(\ell) = \ell+1$ and $F(\ell) = \ell$ for respectively internal and external sources. The characteristic timescales of equations 5, 7 and 8 are parameterized by $\tau_i(\ell) = M_i\ell^{-\alpha_i}$.

Field	Spectrum	radius a (km)	A (nT)	M	α
Core	Flat	3456	D: 1.12×10^5 9.74×10^4	$\tau_c(1)$: 935 yrs $M(\ell \geq 2) = 514$ yrs	1.06
Lithospheric	C-Based	6287	0.16	∞	0
Close magnetospheric	C-Based	12524	D: 9.16 1.88	$\tau_m(1)$: 1.54 days $M(\ell \geq 2) = 18$ min	0
Remote magnetospheric	C-Based	235570	7.3	10.31 yrs	0
Fluctuating magnetospheric	C-Based	13028	D: 3 4.56	$\tau_{fm}(1)$: 0.36 day $\tau_{fm}(2)$: 0.55 days $M(\ell \geq 3) = 4$ days	1.15
Residual ionospheric/ induced	Flat	6324	D: 5.48 4.39	$\tau_i(1)$: 0.71 day $M(\ell \geq 2) = 1.76$ day	0.93
Field-aligned currents	C-Based	7917	D: 0 1.22	$\tau_{fac}(1)$: 0 $M(\ell \geq 2) = 1$ min	0

271 last sources are the external magnetospheric fields, which we model with a close (g_m), a remote (g_{rm})
272 and a fluctuation components (g_{fm}). Together they exhibit a strong dipole and their energy spectra are
273 rapidly decaying.

274 The different sources cover a large variety of timescales, ranging from minutes to centuries. For the core
275 field, the characteristic time associated with its non dipolar part reads $\tau_c(\ell) = 514\ell^{-1.06}$. This power law
276 is close to the slower estimate of *Lhuillier et al. (2011)* given by $\tau(\ell) = 470\ell^{-1}$, but suggests about 10%
277 longer time scales. For the core dipole, the estimation algorithm yields $\tau_c(1) = 935$ years. Since we only
278 consider data over a 17 year period, this estimate is likely not very precise but nevertheless illustrates
279 that the dipole evolves much slower than the other harmonics. The residual ionospheric and induced
280 fields vary very rapidly in comparison, with time scales between one hour and one day, independent of
281 the length scale. Sometimes assumed to be static (see *Olsen et al. (2014)*; *Finlay et al. (2016)*), the
282 remote magnetospheric field has a time scale of $\tau_{rm} \sim 10.3$ years in our study, a value close to the solar
283 cycle. The part of the external fields typically associated with the ring current are the degree $\ell = 1$
284 contribution of the close and fluctuating magnetospheric fields. Whereas the purely zonal part g_m
285 exhibits a characteristic timescale of $\tau_m(1) = 1.5$ days, the fluctuating part g_{fm} , assumed to have SH
286 order $m = \{0, 1, -1\}$ here, varies faster with $\tau_{fm}(1) \sim 8$ hours. For the small scales magnetospheric field,
287 the time scales of the zonal contributions are shorter than those of the degree one contributions. Note
288 that for g_m , $\tau_m(\ell \geq 2) = 18$ minutes, a characteristic time lower than the 30 minutes time step of the
289 Kalman filter algorithm. In such a case, where the estimation of τ was leading to lower values than the
290 algorithm time step, the slope of the parameterized timescale was set to zero, and the source was only
291 characterized by a spatio-temporal covariance structure of the form given by equation 5. Its evolution
292 from one time step to the other was also treated as a temporal white noise. Finally, the fastest varying
293 source is the field-aligned currents with $\tau_{fac}(\ell) = 1$ minute. Together with the non dipolar part of g_m ,
294 g_{fac} , with its zonal structure and short memory of its past, strongly resembles the observed disturbance
295 along satellite tracks discussed in *Finlay et al. (2017)*, and generally affecting the construction of small
296 scale lithospheric field models (see *Thébault et al. (2017)*).

297 **Model results**

298 The optimal model parameters described in the previous section are fixed in the sequential Kalman filter
299 assimilation. The model seeks to describe the data with the spherical harmonics source coefficients $g_i(t)$,
300 which we call the Kalmag geomagnetic field model. Because the parameters were derived from data at

301 low geomagnetic activity, we also have to restrict the final model data. This is done on the fly by testing
302 how much a forecast differs from the data. Whenever the difference lies outside the 95.4% confidence
303 interval predicted by the slow varying sources (the ones exhibiting some characteristic time larger or
304 equal than a day at some degree ℓ) the associated data points are dismissed. All in all, 28.6% of the
305 originally selected data (see section **Data**) were dismissed.

306 We recall that the forecast time step is set to 30 minutes. The entire model (mean and covariance of
307 \mathbf{z}) is stored every 0.25 year, although outputs could be saved down to every time steps. Figure 2 shows
308 the Kalmag energy spectra at the Earth’s surface for the core and the lithospheric field for the epoch
309 2015.0. For degree $\ell \leq 15$, the standard deviations (SD) of both fields are comparable and exceed the
310 mean value of the lithospheric field. Moreover, the SD of the combined field is smaller than the SD of
311 the individual fields. This illustrates that we cannot separate core and lithospheric contribution at these
312 large scales. It also indicates that the prior level of variance of the lithospheric field, as estimated in the
313 previous section, is therefore simply the extrapolation of the small scale stationary spectrum towards the
314 larges sales.

315 Figure 3 compares energy spectra for three types of solutions for the main field (left) and the secular
316 variation (right) in 2015.0. The Kalman filter solution (thin gray lines and symbols), the solution after the
317 smoothing algorithm (thick black lines and symbols), and a third solution for a 5 year forecast from 2010.0
318 (thin black lines and symbols). Continuous lines show the mean, dashed lines the standard deviation,
319 triangles the differences to the DGRF-13 final field model, and circles the difference to the CHAOS-6.9
320 SV model.

321 Not surprisingly, the forecast yields the largest uncertainties. The smallest uncertainties are achieved
322 in the smoothed solution, since the smoothing process allows to take information from the future into
323 account. For the field itself, the fact that the differences to the DGRF-13 final model are similar to the
324 model uncertainties, indicates that these uncertainties are reliably estimated. For the secular variation,
325 the predicted uncertainty levels seems to be slightly overestimated, at least for the Kalman filter and the
326 smoothing solutions. The maximum resolution achieved for the SV is $\ell = 16$ for the smoothing solution,
327 beyond this value the SD becomes larger that the mean signal.

328 On figure 4 are displayed various estimations of the radial (left), azimuthal (middle) and longitudinal
329 (right) secular variation at the level of several ground based observatories over the period 2000.0 – 2025.0.
330 Blue dots correspond to SV estimations deriving from ground based observatory measurements. They are

331 obtained by taking annual differences of the measured magnetic field averaged over 0.1 years. The black
332 lines are evaluations of the SV through the CHAOS-6.9 model. The blue and yellow lines are respectively
333 the IGRF-13 secular variation and the Kalmag candidate SV. The red area is the Kalmag mean secular
334 variation plus and minus 2 standard deviation (σ). Between 2000.6 and 2020.33 the outcomes of the
335 smoothing solution are shown whereas outside this time window the secular variation is estimated with
336 the forecast step the Kalman filter. Finally, the red dashed lines are the mean SV $\pm 2\sigma$ coming from 5
337 year forecast simulations.

338 The first observation one can make is that whenever the secular variation deriving from observatory
339 data exhibits a smooth evolution, the latter is well reproduced by the Kalmag model. We can also
340 notice that at least until 2019.0, the CHAOS-6.9 SV is always lying within 95.4% confidence interval
341 ($E[\partial_t B] \pm 2\sigma$) predicted by our model. Because the Kalmag model is only deriving from the CHAMP
342 and SWARM measurements, data are missing between 2010.7 and 2013.8. This translates into a global
343 increase of uncertainty predictions as it can clearly be witnessed for the longitudinal component of the
344 SV in Mawson or Tuntungan. However, with the combination of the Kalman filter with the smoothing
345 algorithm, the data gap does not lead to any particular issue to connect the two satellite eras since such
346 an approach enables us to account for any space time correlations. As already shown through the energy
347 spectra of figure 3, the forecast algorithm is quite accurate to predict the future states of the secular
348 variation. The three hindcast simulations covering the periods 2005 – 2010, 2010 – 2015 and 2015 – 2020
349 are a confirming it. Nevertheless, in particular locations where the SV exhibits rapid variations as in
350 M’Bour, the simple auto regressive dynamics propagating the core field, fails to not only reproduce but
351 also bound the real evolution of the SV. This calls for using more complex forecast models, able for
352 example to account for the nonlinear interactions between the core field and a time dependent outer core
353 flow as in *Barrois et al. (2017)*; *Bärenzung et al. (2018)*; *Sanchez et al. (2019)*. For the incoming 5 years,
354 both the IGRF-13 or our candidate SV models (which are everywhere quite close to one another) are lying
355 well between the $\pm 2\sigma$ predicted error bars of the updated Kalmag model. In M’Bour however, recent
356 observations tend to show a rapid increase of the azimuthal component of the SV. If it is not followed by
357 a decrease, core field predictions at this location using the IGRF model may rapidly deviate from reality.
358 The last result analyzed in this study, is a comparison of the different candidates for the IGRF-13 main
359 field in 2020.0, and the field as it can be evaluated with measurements taken after 2020.0. As shown
360 with figure 3 and discussed previously, the accuracy of the model deriving from the smoothing algorithm,

361 which takes into account knowledge beyond the epoch of evaluation, is higher than the Kalman filter
362 solution where the model derivation only accounts for previously assimilated data. We could also observe
363 that the longer the forecasts the lower the accuracy of the model. For the construction of the IGRF-13
364 model, measurements were only available up to maximum 2019.75, so the difference between the updated
365 Kalmag model (which derives from data assimilated up to 2020.33) and the various candidates can be
366 considered as the errors of the candidates predictions. These errors are displayed in figure 5 through their
367 energy spectra evaluated at the Earth’s surface. Whereas the error spectrum of the Kalmag candidate
368 is drawn with a thick black line, the ones associated with the other candidates are shown with thin gray
369 lines. Because the Kalmag model may exhibit a permanent bias, the difference between the model and
370 the candidate may represent an erroneous evaluation of the error. Therefore the candidates errors were
371 also computed using another model taking recent data into account (up to March 2020), the CHAOS-7.2
372 model of *Finlay et al. (2020)* which is also, in its first version, the parent model of the DTU candidate
373 for IGRF-13. The spectra of these error evaluations are shown with dashed lines on figure 5. When
374 compared to the Kalmag model, the Kalmag candidate appears to be the most accurate prediction of the
375 main field in 2020.0 with an error level lower than every other candidate at any SH degree ℓ . When the
376 comparison is performed with the CHAOS-7.2 model, the Kalmag candidate globally remains the most
377 precise estimation of the 2020.0 field up to $\ell = 8$. However, at smaller scales the DTU candidate is closer
378 to its parent model CHAOS-7.2, but the level of approximated error of the Kalmag candidate remains
379 extremely low.

380 **Conclusion**

381 We presented in this study a new approach to derive a Geomagnetic field model from direct measurements
382 of the Earth’s magnetic field. Performing sequentially in time, the Kalmag model, which is the
383 combination of a Kalman filter and a smoothing algorithm, enables us to consider complex prior covariance
384 structure to characterize both spatially and temporally the different magnetic sources composing the
385 observable field. The evaluation of the parameters controlling the statistical properties of each modeled
386 source reveals the large variety of spatial and timescales populating the Earth’s magnetic field, and
387 reinforces the idea of treating the assimilation of geomagnetic data sequentially in time. By allowing the
388 presence of a large scale lithospheric field independent from the core field, we could show that with the
389 prior characterization we chose, the two sources could not be separated. Furthermore, although the sum

390 of the two fields can be very accurately estimated, the level of uncertainty associated with each individual
391 source is directly linked to the prior variance of the lithospheric field. This implies a maximum resolution
392 for the core field of spherical harmonics degree $\ell \sim 15$. Its time derivative however can be accurately
393 estimated up to $\ell = 16$. Globally, the model provides reliable uncertainty quantification for whether
394 past, present or future field estimates. It also permits, through the spatio temporal correlations a priori
395 imposed, to consistently connect the CHAMP and the SWARM satellite eras.

396 For short term forecasts, as the derivation of the IGRF model requires it, we could observe that our
397 approach can be more accurate than other existing methods. This is certainly due to the fact that the
398 secular variation is estimated through its dynamical correlation with the core field and is not a fit to
399 the past evolution. There is nevertheless still some room for improvement. Considering more physically
400 based dynamical equations to constrain the evolution of the various fields, such as dynamo simulations for
401 the core field, would certainly improve the separation of the different sources, and provide more accurate
402 predictions of future states. The temporal window covered by the model could also be extended by taking
403 data from previous satellite missions but also ground based observatories or magnetic surveys.

404 **List of abbreviations**

- 405 • SH: Spherical harmonics.
- 406 • SV: Secular variation.
- 407 • SD: Standard deviation.

408 **Funding**

409 This work has been funded by the German Research Foundation (DFG) within the Priority Program
410 SPP1788 “Dynamic Earth”.

411 **Availability of data and materials**

412 Champ data can be downloaded at <https://isdc.gfz-potsdam.de/champ-isdc/access-to-the-champ-data/>

413 Swarm data can be downloaded at ftp://swarm-diss.eo.esa.int/Level1b/Entire_mission_data/MAGx_LR/

414 The Kp index can be downloaded at <ftp://ftp.gfz-potsdam.de/pub/home/obs/kp-ap/>

415 The IMF indices can be downloaded at https://spdf.gsfc.nasa.gov/pub/data/omni/low_res_omni/

416 The model presented here is available upon request.

417 **Competing interests**

418 The authors declare that they have no competing interests.

419 **Author’s contributions**

420 Baerenzung Julien produced the Kalmag model. Holschneider Matthias contributed to the theoretical
421 developments. Lesur Vincent provided his expertise on satellite data, and the algorithms to calculate the
422 different coordinate transforms required for the model. Wicht Johannes and Sanchez Sabrina participated
423 to the elaboration of the model requirements, and to the redaction of the manuscript.

424 **Acknowledgments**

425 This work has been supported by the German Research Foundation (DFG) within the Priority Program
426 SPP1788 “Dynamic Earth”.

427 **References**

- 428 Bärenzung, J., M. Holschneider, J. Wicht, S. Sanchez, and V. Lesur (2018), Modeling and Predicting
429 the Short-Term Evolution of the Geomagnetic Field, *Journal of Geophysical Research (Solid Earth)*,
430 *123*(6), 4539–4560, doi:10.1029/2017JB015115.
- 431 Barrois, O., N. Gillet, and J. Aubert (2017), Contributions to the geomagnetic secular variation from a
432 reanalysis of core surface dynamics, *Geophysical Journal International*, *211*(1), 50–68,
433 doi:10.1093/gji/ggx280.
- 434 Bouligand, C., N. Gillet, D. Jault, N. Schaeffer, A. Fournier, and J. Aubert (2016), Frequency spectrum
435 of the geomagnetic field harmonic coefficients from dynamo simulations, *Geophysical Journal
436 International*, *207*, 1142–1157, doi:10.1093/gji/ggw326.
- 437 Christensen, U. R., and A. Tilgner (2004), Power requirement of the geodynamo from ohmic losses in
438 numerical and laboratory dynamos, *nature*, *429*, 169–171, doi:10.1038/nature02508.
- 439 De Santis, A., D. R. Barraclough, and R. Tozzi (2003), Spatial and temporal spectra of the geomagnetic
440 field and their scaling properties, *Physics of the Earth and Planetary Interiors*, *135*, 125–134,
441 doi:10.1016/S0031-9201(02)00211-X.
- 442 Finlay, C. C., N. Olsen, S. Kotsiaros, N. Gillet, and L. Tøffner-Clausen (2016), Recent geomagnetic
443 secular variation from Swarm and ground observatories as estimated in the CHAOS-6 geomagnetic

444 field model, *Earth, Planets, and Space*, 68, 112, doi:10.1186/s40623-016-0486-1.

445 Finlay, C. C., V. Lesur, E. Thébault, F. Vervelidou, A. Morschhauser, and R. Shore (2017), Challenges
446 Handling Magnetospheric and Ionospheric Signals in Internal Geomagnetic Field Modelling, *Space*
447 *Science Reviews*, 206(1-4), 157–189, doi:10.1007/s11214-016-0285-9.

448 Finlay, C. C., C. Kloss, N. Olsen, M. Hammer, and L. Tøffner-Clausen (2020), DTU candidate models
449 for IGRF-13, *Earth, Planets, and Space*.

450 Gillet, N., D. Jault, C. C. Finlay, and N. Olsen (2013), Stochastic modeling of the Earth’s magnetic
451 field: Inversion for covariances over the observatory era, *Geochemistry, Geophysics, Geosystems*, 14,
452 766–786, doi:10.1002/ggge.20041.

453 Gillet, N., D. Jault, and C. C. Finlay (2015), Planetary gyre, time-dependent eddies, torsional waves,
454 and equatorial jets at the Earth’s core surface, *Journal of Geophysical Research (Solid Earth)*, 120,
455 3991–4013, doi:10.1002/2014JB011786.

456 Holschneider, M., V. Lesur, S. Mauerberger, and J. Baerenzung (2016), Correlation-based modeling and
457 separation of geomagnetic field components, *Journal of Geophysical Research (Solid Earth)*, 121,
458 3142–3160, doi:10.1002/2015JB012629.

459 Hulot, G., and J. L. Le Mouél (1994), A statistical approach to the Earth’s main magnetic field, *Physics*
460 *of the Earth and Planetary Interiors*, 82(3-4), 167–183, doi:10.1016/0031-9201(94)90070-1.

461 Jackson, A., A. R. T. Jonkers, and M. R. Walker (2000), Four centuries of geomagnetic secular
462 variation from historical records, in *Astronomy, physics and chemistry of H^+ ₃*, *Philosophical*
463 *Transactions of the Royal Society of London Series A*, vol. 358, p. 957, doi:10.1098/rsta.2000.0569.

464 Kalman, R. E. (1960), A New Approach to Linear Filtering and Prediction Problems, *Journal of Basic*
465 *Engineering*, 82, 35–45, doi:10.1115/1.3662552.

466 Lesur, V., I. Wardinski, M. Rother, and M. Mandea (2008), GRIMM: the GFZ Reference Internal
467 Magnetic Model based on vector satellite and observatory data, *Geophysical Journal International*,
468 173, 382–394, doi:10.1111/j.1365-246X.2008.03724.x.

469 Lesur, V., I. Wardinski, M. Hamoudi, and M. Rother (2010), The second generation of the GFZ
470 Reference Internal Magnetic Model: GRIMM-2, *Earth, Planets, and Space*, 62, 765–773,
471 doi:10.5047/eps.2010.07.007.

472 Lesur, V., K. Whaler, and I. Wardinski (2015), Are geomagnetic data consistent with stably stratified
473 flow at the core-mantle boundary?, *Geophysical Journal International*, 201, 929–946,

474 doi:10.1093/gji/ggv031.

475 Lesur, V., I. Wardinski, J. Baerenzung, and Holschneider (2017), On the frequency spectra of the core
476 magnetic field Gauss coefficients, *Physics of the Earth and Planetary Interiors*,
477 doi:<https://doi.org/10.1016/j.pepi.2017.05.017>.

478 Lhuillier, F., J. Aubert, and G. Hulot (2011), Earth’s dynamo limit of predictability controlled by
479 magnetic dissipation, *Geophysical Journal International*, *186*, 492–508,
480 doi:10.1111/j.1365-246X.2011.05081.x.

481 Maus, S., H. Lühr, G. Balasis, M. Rother, and M. Manda (2005), *Introducing POMME, the POTSdam*
482 *Magnetic Model of the Earth*, p. 293, doi:10.1007/3-540-26800-6_46.

483 Maus, S., C. Manoj, J. Rauberg, I. Michaelis, and H. Lühr (2010), NOAA/NGDC candidate models for
484 the 11th generation International Geomagnetic Reference Field and the concurrent release of the 6th
485 generation Pomme magnetic model, *Earth, Planets, and Space*, *62*, 729–735,
486 doi:10.5047/eps.2010.07.006.

487 Olsen, N., H. Lühr, T. J. Sabaka, M. Manda, M. Rother, L. Tøffner-Clausen, and S. Choi (2006),
488 CHAOS-a model of the Earth’s magnetic field derived from CHAMP, Oersted, and SAC-C magnetic
489 satellite data, *Geophysical Journal International*, *166*, 67–75, doi:10.1111/j.1365-246X.2006.02959.x.

490 Olsen, N., H. Lühr, C. C. Finlay, T. J. Sabaka, I. Michaelis, J. Rauberg, and L. Tøffner-Clausen (2014),
491 The CHAOS-4 geomagnetic field model, *Geophysical Journal International*, *197*, 815–827,
492 doi:10.1093/gji/ggu033.

493 Olsen, N., D. Ravat, C. C. Finlay, and L. K. Kother (2017), LCS-1: a high-resolution global model of
494 the lithospheric magnetic field derived from CHAMP and Swarm satellite observations, *Geophysical*
495 *Journal International*, *211*(3), 1461–1477, doi:10.1093/gji/ggx381.

496 Rauch, H. E., C. T. Striebel, and F. Tung (1965), Maximum likelihood estimates of linear dynamic
497 systems, *AIAA Journal*, *3*(8), 1445–1450, doi:10.2514/3.3166.

498 Ropp, G., V. Lesur, J. Baerenzung, and M. Holschneider (2020), Sequential modelling of the Earth’s
499 core magnetic field, *Earth, Planets, and Space*.

500 Sabaka, T. J., N. Olsen, and R. A. Langel (2002), A comprehensive model of the quiet-time, near-Earth
501 magnetic field: phase 3, *Geophysical Journal International*, *151*, 32–68,
502 doi:10.1046/j.1365-246X.2002.01774.x.

503 Sabaka, T. J., N. Olsen, R. H. Tyler, and A. Kuvshinov (2015), CM5, a pre-Swarm comprehensive

504 geomagnetic field model derived from over 12 yr of CHAMP, Oersted, SAC-C and observatory data,
505 *Geophysical Journal International*, 200, 1596–1626, doi:10.1093/gji/ggu493.

506 Sabaka, T. J., L. Tøffner-Clausen, N. Olsen, and C. C. Finlay (2018), A comprehensive model of
507 Earth’s magnetic field determined from 4 years of Swarm satellite observations, *Earth, Planets, and*
508 *Space*, 70, 130, doi:10.1186/s40623-018-0896-3.

509 Sabaka, T. J., L. Tøffner-Clausen, N. Olsen, and C. C. Finlay (2020), CM6: a comprehensive
510 geomagnetic field model derived from both CHAMP and Swarm satellite observations, *Earth,*
511 *Planets, and Space*, 72(1), 80, doi:10.1186/s40623-020-01210-5.

512 Sanchez, S., J. Wicht, J. Bärenzung, and M. Holschneider (2019), Sequential assimilation of
513 geomagnetic observations: perspectives for the reconstruction and prediction of core dynamics,
514 *Geophysical Journal International*, 217(2), 1434–1450, doi:10.1093/gji/ggz090.

515 Sugiura, M. (1963), *Hourly values of equatorial Dst for the IGY*, Greenbelt, Md, NASA, Goddard
516 Space Flight Center.

517 Thébaud, E., V. Lesur, K. Kauristie, and R. Shore (2017), Magnetic Field Data Correction in Space for
518 Modelling the Lithospheric Magnetic Field, *Space Science Reviews*, 206(1-4), 191–223,
519 doi:10.1007/s11214-016-0309-5.

520 Waters, C. L., B. J. Anderson, and K. Liou (2001), Estimation of global field aligned currents using the
521 iridium® System magnetometer data, *Geophysical Research Letters*, 28(11), 2165–2168,
522 doi:10.1029/2000GL012725.

Figures

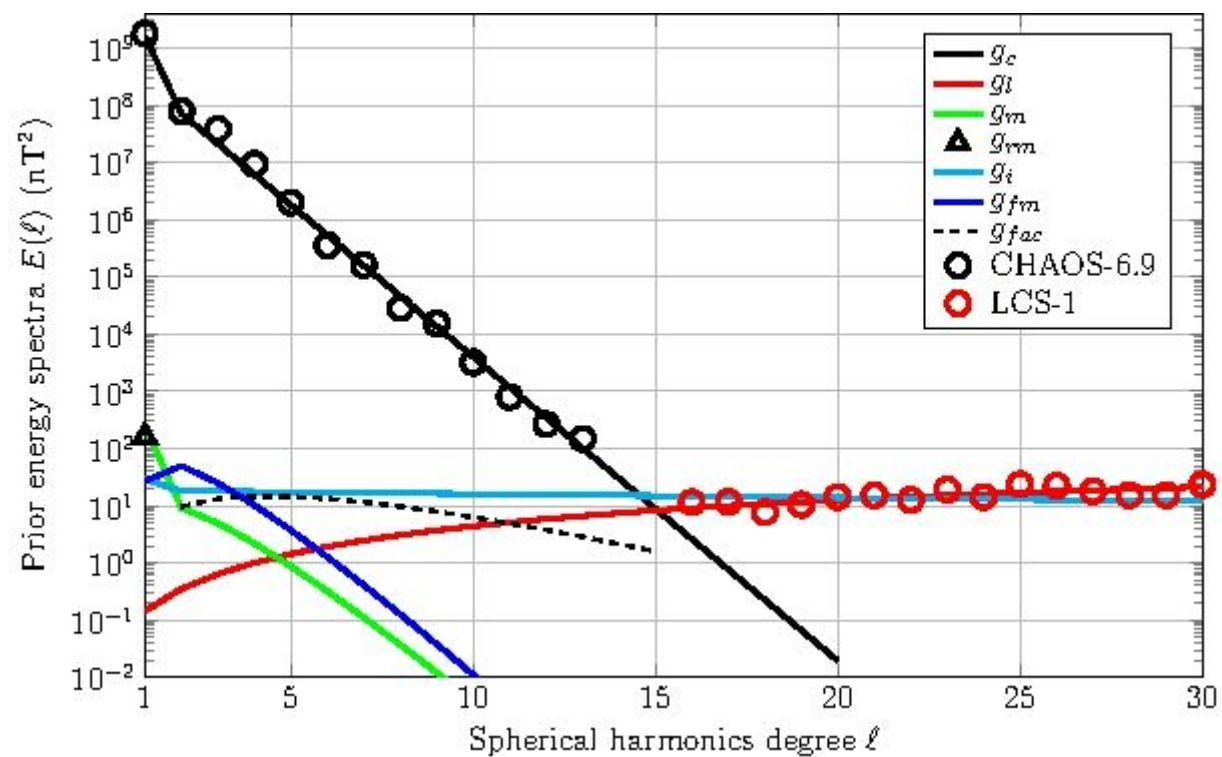


Figure 1

Figure 1

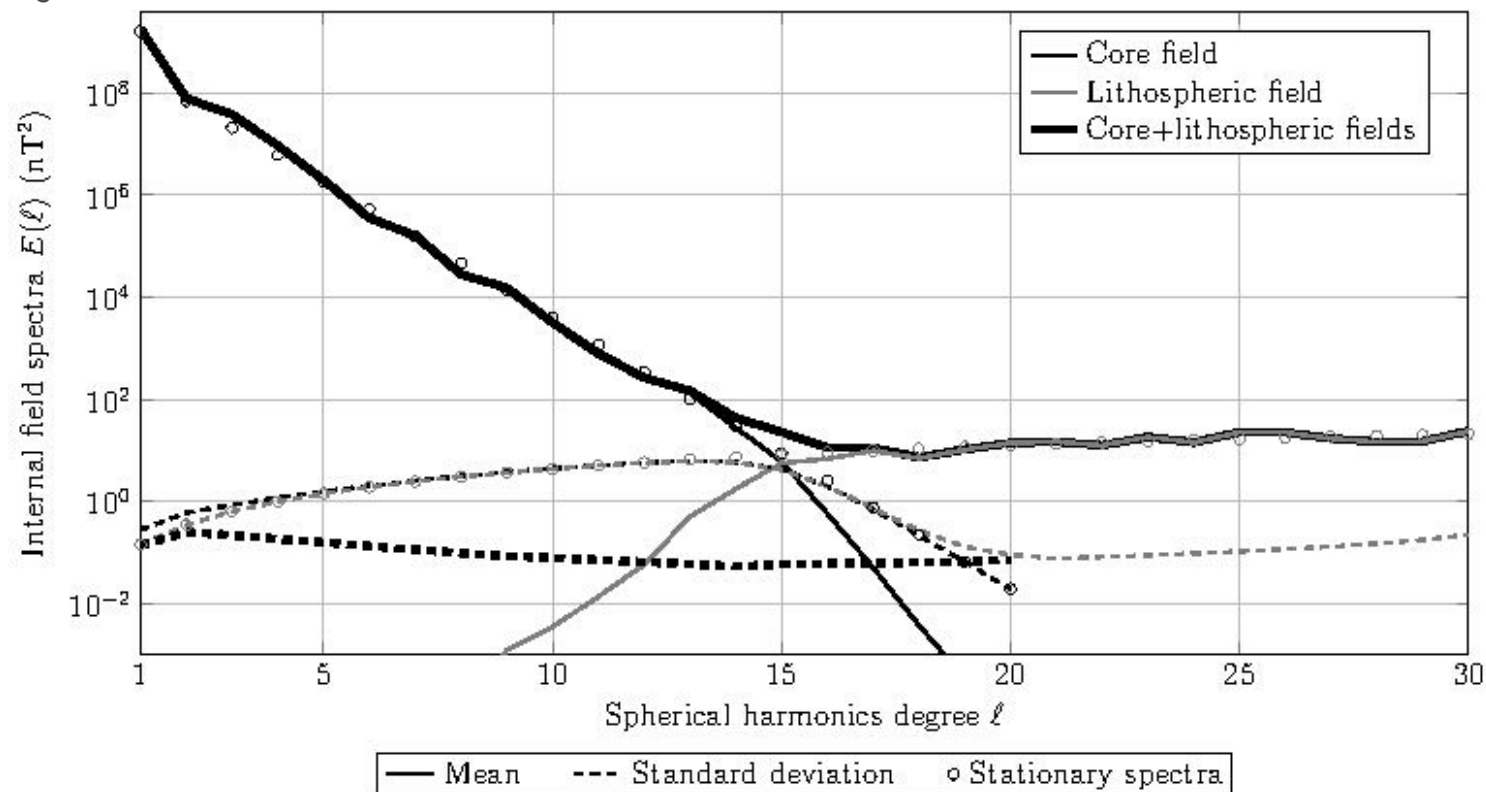


Figure 2

Figure 2

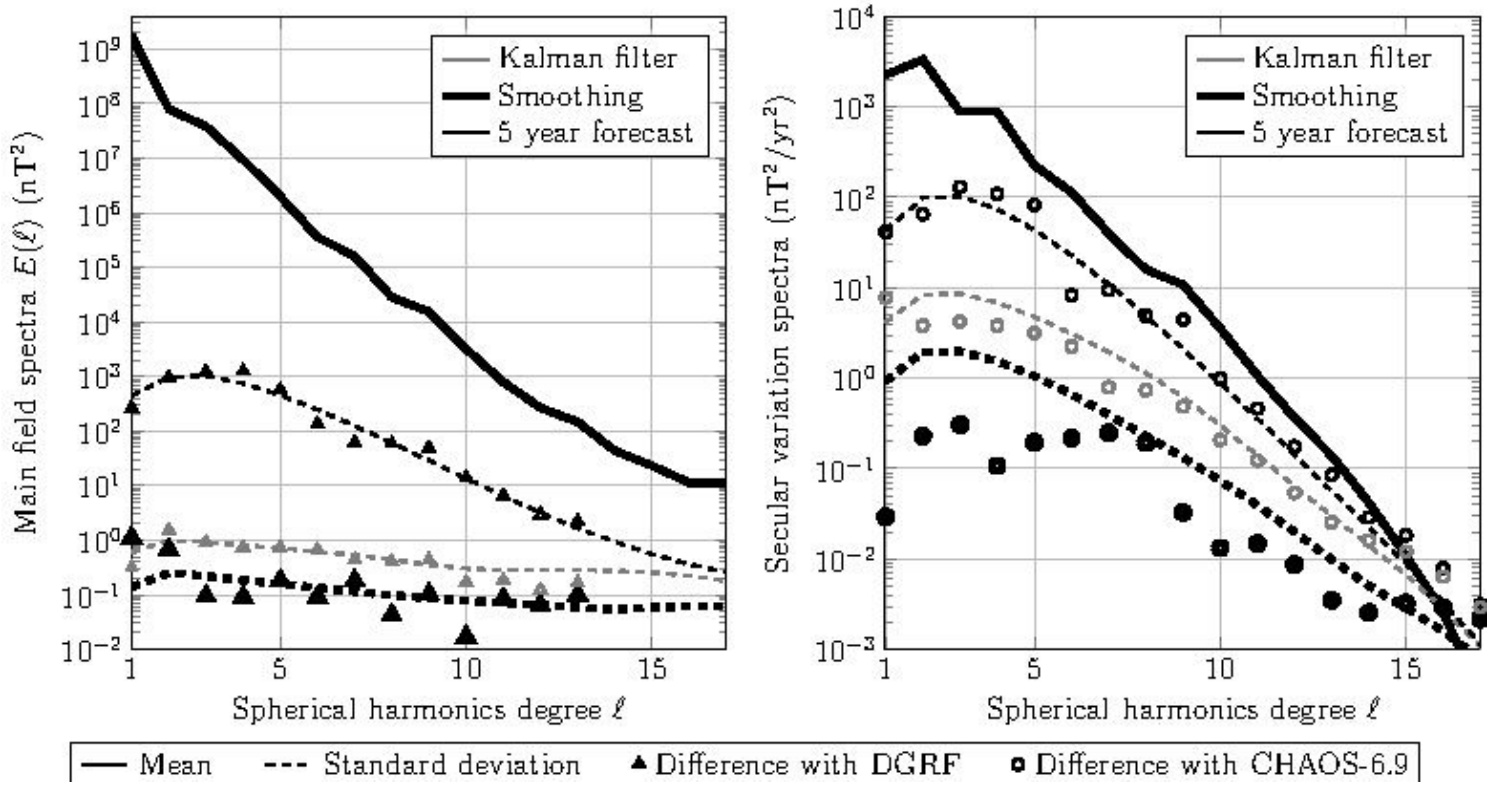


Figure 3

Figure 3

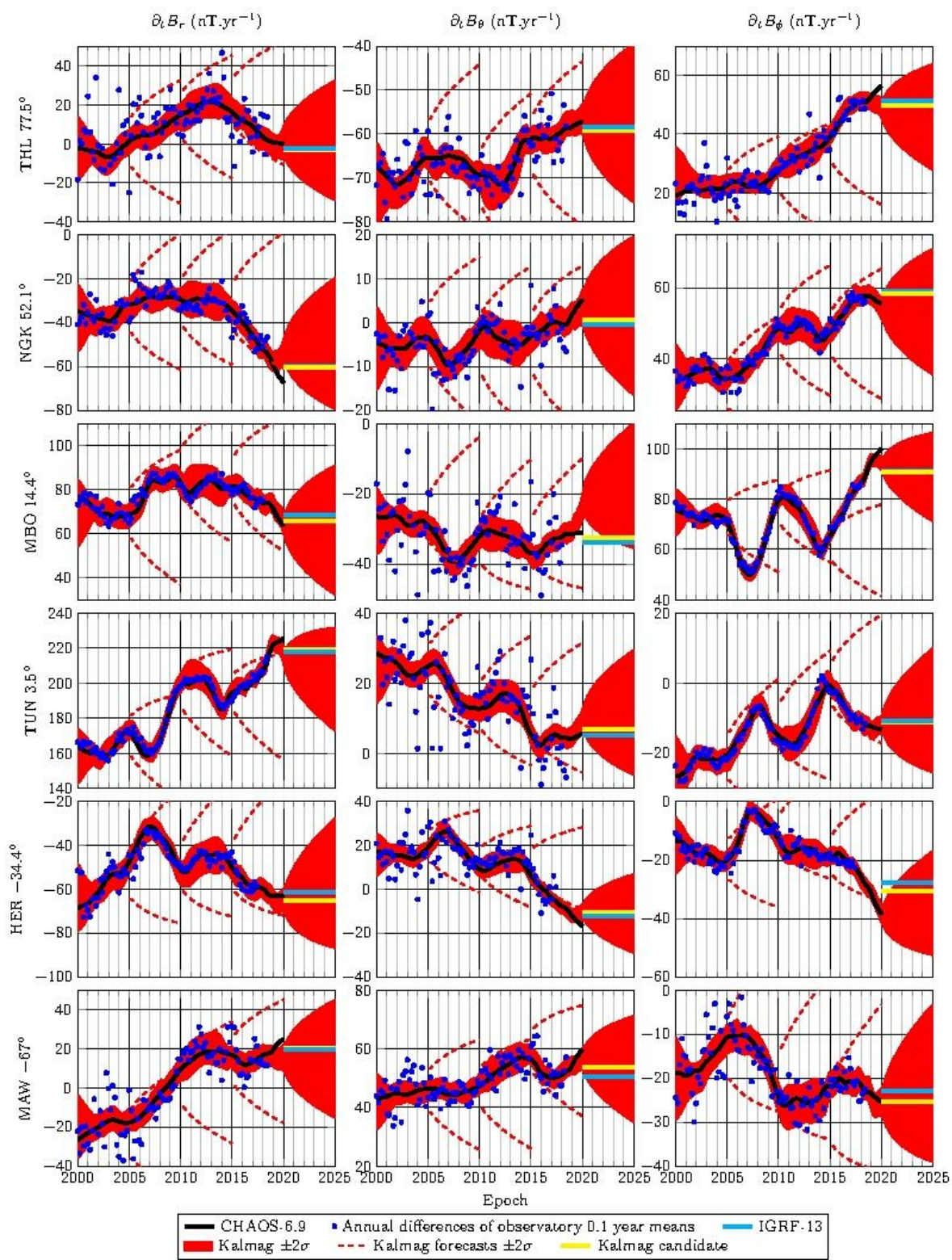


Figure 4

Figure 4

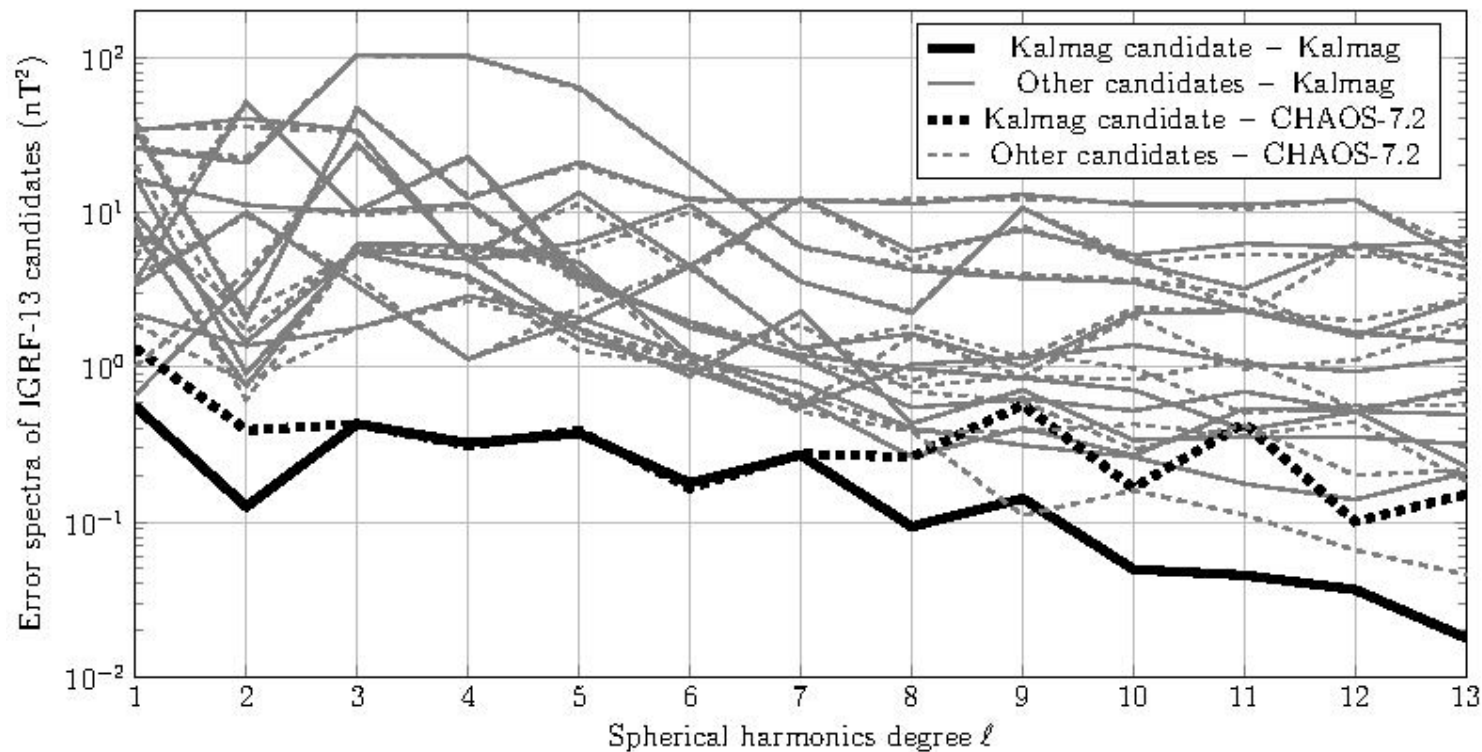


Figure 5

Figure 5

Supplementary Files

This is a list of supplementary files associated with this preprint. Click to download.

- [pictureFile.tex](#)
- [eps.cls](#)
- [manuscript.tex](#)
- [graphicalAbstract.jpg](#)